JGR Atmospheres

RESEARCH ARTICLE
10.1029/2020JD033172

Impacts of Greenland Block Location on Clouds and Surface Energy Fluxes Over the Greenland Ice Sheet

Jamie L. Ward[1], **Mark G. Flanner**[1], **and Etienne Dunn-Sigouin**[2]

[1]Department of Climate and Space Sciences and Engineering, University of Michigan, Ann Arbor, MI, USA, [2]Geophysical Institute, University of Bergen and Bjerknes Center for Climate Research, Bergen, Norway

Key Points:
- Greenland-wide cloud reduction produced by northern block days is at least four times greater than southern Greenland block days
- Block-based cloud reductions produce negative Greenland-wide total cloud radiative forcing changes for all Greenland block quadrants
- Total surface energy blocking changes are influenced more by radiative (nonradiative) fluxes during western (eastern) Greenland block days

Supporting Information:
- Supporting Information S1

Correspondence to:
J. L. Ward,
jamiewa@umich.edu

Citation:
Ward, J. L., Flanner, M. G., & Dunn-Sigouin, E. (2020). Impacts of Greenland block location on clouds and surface energy fluxes over the Greenland ice sheet. *Journal of Geophysical Research: Atmospheres*, *125*, e2020JD033172. https://doi.org/10.1029/2020JD033172

Received 26 MAY 2020
Accepted 25 OCT 2020
Accepted article online 31 OCT 2020

Author Contributions:
Conceptualization: Jamie L. Ward, Mark G. Flanner
Data curation: Jamie L. Ward
Formal analysis: Jamie L. Ward
Investigation: Jamie L. Ward
Methodology: Jamie L. Ward, Mark G. Flanner, Etienne Dunn-Sigouin
Resources: Jamie L. Ward
Supervision: Mark G. Flanner
Visualization: Jamie L. Ward
Writing – original draft: Jamie L. Ward
Writing – review & editing: Mark G. Flanner, Etienne Dunn-Sigouin

Abstract Clouds and blocking activity have been implicated as causes of increased Greenland Ice Sheet (GrIS) melt in the 21st century. Although Greenland blocks (i.e., long-lasting, mostly stationary anticyclones) generally reduce cloud cover and move warm air over Greenland, the elevated GrIS perturbs air and moisture transport in complex ways, implying a need to better understand how blocks affect cloud and surface energy flux anomaly patterns. In this study, we use a combination of daily MODIS cloud data and meteorological and energy flux data from MERRA-2 reanalysis to better understand how Greenland block location, separated into four equal-area quadrants, affects regional cloud and surface energy flux spatial patterns in the summer months of 2002–2018. Overall, cloud fraction and cloud water path reductions are approximately four times greater during northern block days than southern block days. Net cloud radiative forcing anomalies are negative for all Greenland block locations because negative longwave cloud radiative forcing anomalies exceed positive shortwave cloud radiative forcing changes. However, greater cloud cover reductions during northern block days produce more negative net cloud radiative forcing anomalies than southern block days. Greenland-average (i.e., latitude-weighted average of all GrIS grids) net surface energy flux anomalies range from +7 to +12W/m^2 for all block quadrants. While net shortwave energy anomalies dominate the total surface energy response during western Greenland block days, sensible heating is responsible for approximately half of positive total surface energy change during eastern Greenland block days.

1. Introduction

Many atmospheric processes affect Greenland Ice Sheet (GrIS) surface energy fluxes and subsequent surface mass balance changes. Clouds impact the GrIS surface by reflecting insolation away from the surface (i.e., cooling) while also trapping and reemitting longwave energy (i.e., warming). Over snow-covered surfaces like the GrIS, the magnitude of this cloud radiative forcing is affected by cloud properties like ice-to-liquid cloud content ratios, cloud height, and cloud water path (i.e., Shupe & Intrieri, 2004). Liquid-bearing clouds, which are most common over Greenland during the summer months (Lenaerts et al., 2017; Miller et al., 2015; Shupe et al., 2013; Van Tricht et al., 2016), enhance net radiative surface energy flux by largely increasing longwave energy fluxes and only marginally dimming surface insolation (McIlhattan et al., 2017; Shupe & Intrieri, 2004). Optically thin, low-lying liquid-bearing clouds are optimal for increasing surface radiative energy flux (Bennartz et al., 2013; Van Tricht et al., 2016). In recent years and in future climate projections, liquid-bearing clouds contribute to melt over much of the GrIS (Bennartz et al., 2013; Hofer et al., 2019; Van Tricht et al., 2016).

One factor that increases Greenland cloud fraction is enhanced atmospheric water vapor from local- and remotely sourced moisture transport (Ballinger et al., 2019; Johansson et al., 2017). Although summertime moisture amounts and source regions vary regionally over Greenland (e.g., Nusbaumer et al., 2019), a large portion of atmospheric water vapor originates over the North Atlantic. This warmer, moister air moves over the GrIS surface and can influence not only clouds but also skin surface temperatures and snowmelt rate (Mattingly et al., 2018; Pfahl et al., 2015). Over the last 20 years, available water vapor over Greenland has increased with warming air temperatures (Mattingly et al., 2016) and will likely affect Greenland's future climate through surface melt feedbacks related to increased cloud cover.

Atmospheric dynamics affect GrIS surface processes by influencing cloud formation, moisture transport, and temperature advection. These processes are complicated by airflow changes that result because of the elevated GrIS surface. Greenland "blocks" (i.e., quasi-stationary anticyclones lasting for days-to-weeks) increase GrIS melt through warm air advection and cloud suppression (Box et al., 2012; Fettweis et al., 2013; Hanna et al., 2014; Hofer et al., 2017; Mattingly et al., 2018; McLeod & Mote, 2016). The resulting cloud reduction and warm air advection from blocking enhance insolation and sensible heat fluxes, respectively, which can enhance surface melt (Hanna et al., 2014; Hofer et al., 2017; Lim et al., 2016; Mioduszewski et al., 2016; Rajewicz & Marshall, 2014). In addition, Greenland blocking is likely related to regional atmospheric moisture transport processes (i.e., Mattingly et al., 2018; Nusbaumer et al., 2019), and thus also cloud patterns and phase. Over Summit, liquid-bearing clouds have larger cloud water paths and are longer-lived during block-like (i.e., ridging) flow regimes (Edwards-Opperman et al., 2018). Summertime Greenland blocking activity has significantly increased over the past 20 years (i.e., Belleflamme et al., 2015; Fettweis et al., 2013; Hanna et al., 2016, 2018; McLeod & Mote, 2016; Rajewicz & Marshall, 2014) and is another potential contributor to GrIS snowmelt enhancement (Fettweis et al., 2011; Rignot et al., 2008; Shepherd et al., 2012; Tedesco & Fettweis, 2020).

The surface mass balance and energy flux effects resulting from different wind patterns and cloud locations vary spatially over the GrIS. Compared to eastern Greenland, westerly/southerly winds produce more cloud cover over western Greenland in the summer months that significantly reduces insolation while enhancing longwave fluxes and surface melt (Cawkwell & Bamber, 2002; Cullather & Nowicki, 2018). Moisture transport over western Greenland also has a larger impact on local GrIS snowmelt because the air is warmer and moister than over eastern Greenland (Mattingly et al., 2018). The effects of Greenland blocking on cloud cover (e.g., Hofer et al., 2017; Lim et al., 2016), temperature advection, and subsequent snowmelt and surface energy flux processes (e.g., Belleflamme et al., 2015; Fettweis et al., 2013; Noël et al., 2019; Tedesco et al., 2016) also exhibit spatial variability and have been explored in previous studies. However, these studies investigate average blocking conditions that do not account for the quasi-stationary nature of Greenland blocks (e.g., Chen & Luo, 2017). Different block locations could produce variations in cloud, moisture transport, and surface energy flux patterns by changing air source regions and how block airflow interacts with the GrIS surface, which could directly impact GrIS surface mass balance processes.

In this study, we use a combination of reanalysis and satellite cloud data to document and differentiate the effects of summertime (i.e., June through August) Greenland block location on cloud formation, moisture transport, and surface energy flux processes over the GrIS. First, we describe the data sets, blocking detection algorithm, and statistical methods we use for this study. Next, we explore the impacts of block location on cloudiness in terms of moisture transport, temperature, and airflow patterns. We then explore the implications of cloud changes on Greenland-wide cloud radiative forcing and total surface energy fluxes.

2. Methods

2.1. Greenland Block Data and Detection

We use Modern-Era Retrospective Analysis for Research and Applications, version 2 (MERRA-2) reanalysis data to find blocks and analyze their associated meteorological and surface energy flux patterns over the GrIS (Gelaro et al., 2017). Daily averages are calculated from all subdaily MERRA-2 meteorological and surface energy flux fields. Because we are interested in blocking-induced cloud and surface energy flux anomalies that could materially impact summer surface melt, we analyze blocks in June, July, and August (JJA) from 2002 through 2018. We include days in late May and early September if they are part of early June and late August blocking events, respectively.

To detect blocks in the MERRA-2 data set, we use a modified version of the Dunn-Sigouin et al. (2013) algorithm (hereafter referred to as D-S) (see Table 1). The multistep approach of the D-S algorithm requires the satisfaction of multiple conditions to classify events as blocks (Dunn-Sigouin et al., 2013). In brief, the D-S method tracks contiguous groupings of 500 hPa geopotential height anomalies (Z'_{500}) meeting minimum preestablished amplitude threshold (A) and area requirements (S) over time. For each latitude/longitude grid, we calculate Z'_{500} between 16 May and 15 September with the following formula:

Table 1
D-S Algorithm Original and Modified Parameters

Threshold	Units	Original D-S	Modified D-S
Duration (D)	Days	5	4
Amplitude (A)	Unitless	1.5	1.2
Spatial Scale (S)	km^2	2.5×10^6	1.0×10^6
Overlap (O)	Percentage	50	50

$$Z'_{500}(n) = Z_{500}(n) - Z_{clim}(n), \quad (1)$$

where $Z_{clim}(n)$ is the climatological average 500 hPa geopotential height at each grid point. Z_{clim} is defined using a Gaussian-weighted, 31-day moving window centered on day n for all 17 years (2002–2018) of 500 hPa geopotential height data. Gaussian weighting places more emphasis on days close to n, incorporating seasonal variability in Z_{500}. In the D-S algorithm, a block is recorded if (1) the Z'_{500} areas between consecutive days overlap (O) by a certain percentage, and (2) these anomalies exist for a predefined number of days (D). Although the original D-S detection algorithm further tests for a Z_{500} gradient reversal equatorward of the block, we do not maintain this requirement because persistent high pressure ridging is a prominent variety of blocking in the Greenland region (Fettweis et al., 2013; Hanna et al., 2014; Tedesco et al., 2016). Notably, we define blocks using a duration of 4 days in the algorithm to detect the July 2012 blocking event (e.g., Tedesco et al., 2013). With this change, the July 2012 block lasts for 7 days (i.e., supporting information Table S3), so we only include blocks lasting at least 5 days in the remainder of our analysis in agreement with previous blocking research (e.g., Häkkinen et al., 2014; McLeod & Mote, 2016). Greenland block detection is sensitive to algorithm structure and threshold values within the algorithm (e.g., Woollings et al., 2018). We use this specific set of parameters because they identify a large number of events while also identifying events that are strong enough to impact the Greenland surface energy budget, like the July 2012 blocking event (e.g., Tedesco et al., 2013). More details about the D-S algorithm can be found in Dunn-Sigouin et al. (2013).

The block location for each block day detected in the modified D-S setup is determined using the equal-area block quadrants defined in Figure 1a (latitude and longitude boundaries for each quadrant are provided in the supporting information section, Table S1). Within the contiguous area of highlighted Z'_{500} grids closest to/over Greenland for each block day, we find the local maximum Z'_{500} latitude/longitude coordinate. We then find its corresponding Z_{500} maximum latitude/longitude grid point and bin it in one of the four Greenland block quadrants (Figure 1a). We look for maximum coordinates in both Z'_{500} and Z_{500} because regions of high geopotential height anomalies may not entirely cover the 500 hPa block area. Because midlatitude ridging can result in Z_{500} center points south of our Greenland domain, we allow Z_{500} to lie marginally outside of the defined block quadrants.

2.2. Greenland Cloud Data

We use Moderate Resolution Imaging Spectroradiometer (MODIS) Terra Collection 6, Level 2 cloud data (product code MOD06), which extends from 2002 to present (Platnick et al., 2017), to analyze cloud conditions during Greenland blocking. We choose MOD06 data because of its high spatial and temporal coverage, as well as its incorporation of processing algorithm improvements for high latitude opaque cloud detection and characterization over the reflective GrIS snow (Ackerman et al., 1998; Liu et al., 2010; Platnick

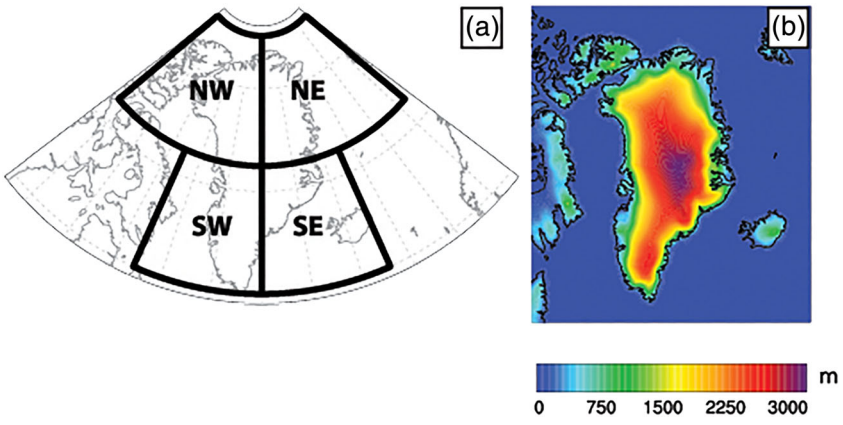

Figure 1. (a) Equal-area Greenland block quadrants. The quadrants are northwest (NW), northeast (NE), southwest (SW), and southeast (SE). (b) Present-day topography of the GrIS derived from MERRA-2 surface geopotential data.

et al., 2017). The cloud water path and cloud optical thickness fields we use are produced by the combination of 1.6 and 2.1 μm bands for better surface-cloud differentiation (Platnick et al., 2001). Although MOD06 data are accompanied by detection uncertainties, we do not include these here.

To better compare the MERRA-2 data to the corresponding daily cloud conditions, we spatially aggregate 1×1 and 5×5 km along-swath gridded granule MOD06 data onto the $0.5° \times 0.625°$ MERRA-2 grid and average all resulting cloud data for each day. This regridded, daily-averaged MOD06 data cover 60 – 85°N latitude and 93.125°W – 13.125°E longitude to accommodate clouds corresponding to blocking in each block quadrant. We first aggregate 1×1 km fields onto the 5×5 km grid for each MODIS granule. Because cloud water path observations are only collected during the day, we exclude "nighttime" pixels with solar zenith angle values exceeding 81.36° for all other cloud variables (Platnick et al., 2017). We then aggregate 5×5 km granule data onto the larger MERRA-2 grid by averaging the closest 5×5 km data points onto each MERRA-2 grid point. Apart from cloud fraction and cloud phase, all MOD06 variables are averaged onto the MERRA-2 grid with cloud fraction weighting for each MODIS granule. Finally, we average (using cloud fraction weighting) each MERRA-2 gridded MOD06 data field over time to create daily average cloud fields.

2.3. Meteorological and Cloud Radiative Forcing Calculations

Because cloud formation depends on the presence of atmospheric moisture, we evaluate moisture transport (kg $m^{-1}s^{-1}$) during blocking in each block quadrant, during all blocks combined, and during nonblock days (i.e., JJA 2002–2018 days that do not exhibit blocking) to gain a first-order understanding of the effects of blocking on clouds and surface processes. Similar to Woods et al. (2013), we calculate daily gridded total column moisture transport as

$$F = \frac{1}{g}\int_{400}^{p_s} Q(p) * W(p)dp. \tag{2}$$

In (2), F is the resulting total column moisture flux, g is the acceleration of gravity (9.8m/s^2), $Q(p)$ is specific humidity at pressure level p, $W(p)$ is the wind velocity at p, and p ranges from pressure at the surface (p_s) to 400 hPa (Woods et al., 2013). We calculate $W(p)$ speed and direction at each grid point using zonal and meridional wind vectors at the corresponding pressure level. Total column wind vectors ($\overrightarrow{\boldsymbol{W}}$) are calculated from pressure-weighted, column-integrated zonal and meridional winds over all pressure levels. Because of GrIS surface elevation variability and daily changes in atmospheric pressure, p_s is spatially and temporally variable in our Greenland domain.

GrIS surface energy balance is important to disentangle the effects of block location and subsequent cloud processes on snowmelt. We calculate total surface energy flux as the sum of net shortwave energy, net longwave energy, sensible heat flux, and latent heat flux at each point in the Greenland domain (e.g., Lenaerts et al., 2019; van den Broeke et al., 2017). We do not include conductive heat flux in our surface energy balance calculation because its magnitude is negligible in ice-covered regions (Yang et al., 2011). In addition, to examine the impacts of clouds in each blocking case on net surface radiative fluxes, we calculate total surface cloud radiative forcing using all-sky (all) and clear-sky (clr) quantities:

$$CRF_{TOTAL} = CRF_{SW} + CRF_{LW} = \left(SW_{net,\,all} - SW_{net,\,clr}\right) + \left(LW_{net,\,all} - LW_{net,\,clr}\right). \tag{3}$$

Because high-latitude insolation varies strongly with time of year, our subsets of regional block and nonblock days are subject to different mean insolation. To account for this, we use MERRA-2 downwelling top-of-atmosphere shortwave energy data to scale surface shortwave flux-related fields so they represent consistent "summer-mean" values. We calculate separate GrIS-wide top-of-atmosphere incoming solar radiation averages for summer (i.e., all days in JJA), "Control" (i.e., JJA nonblock days), and block days belonging to each block quadrant (i.e., "All Blocks," NW, NE, SW, and SE). We divide this summer average by the corresponding "Control" and block day mean insolation to calculate shortwave scaling factors that are used to normalize our filtered surface and cloud shortwave fluxes. These scaling factors are listed in Table S2. Surface energy flux components are considered to be positive in the downward direction because they positively contribute to total surface energy.

We differentiate surface energy fluxes, meteorological conditions, and cloud properties between block days in each quadrant, "All Blocks," and nonblock days ("Control") using two-sample *t* testing for each coordinate and spatial averaging over the GrIS. In the case of spatial averages, we define GrIS pixels as those having at least 50% land ice coverage, as defined with the MERRA-2 land ice surface fractions.

3. Results and Discussion

3.1. Blocking Statistics

Here we briefly describe the frequency characteristics of block days belonging to persistent blocking activity (i.e., blocks lasting at least 5 days from D-S output) for "All Blocks" and individual block quadrants. We find a total of 205 summer block days associated with 30 blocking events. Four of these blocking events extend outside of JJA (see Table S3 for block day list). There are ~12.1 block days per summer, on average, with a standard deviation of ~10.5 days. This year-to-year variability in block day count results from varying synoptic- to planetary-scale dynamics. We find above-average summer block day counts in 2003, 2006–2008, 2012, and 2015–2016 (Figure S1), which aligns well with previously reported Greenland blocking frequencies (e.g., Fettweis et al., 2011, 2013; Hanna et al., 2016; Tedesco et al., 2016).

Binning block days to our defined block quadrants (i.e., Figure 1a) provides us with additional information about preferred blocking regions around Greenland. From Figure 2a, and in agreement with previous studies (i.e., Cullather & Nowicki, 2018; Häkkinen et al., 2014; McLeod & Mote, 2015), the average "All Blocks" block center is located over south-central Greenland. NW and NE blocks are smaller but maintain similar geopotential heights to SW and SE blocks. Overall, we find that the southwest (SW) and southeast (SE) block quadrants contain more block days (69 and 80 days, respectively) than the northwest (NW) and northeast (NE) block quadrants (35 and 21 days, respectively). However, northern quadrant block days constitute 27% of all detected Greenland block days during 2002–2018 and are thus important to Greenland's climate.

3.2. Clouds and Block Location

In this section, we explore MOD06 cloud fraction (Figure 3) and cloud water path changes (Figure S2) over the GrIS for "All Blocks" and individual block quadrants with respect to "Control." We use moisture transport and wind fields (Figure 4) to explain the resulting cloud anomaly patterns for each blocking case. Liquid cloud fraction, ice cloud fraction, cloud top height, cloud top temperature, and cloud optical thickness are all included in the supporting information.

We can see in Figure 3 that cloud fraction anomaly distributions are different between "All Blocks" and individual block quadrants. Regardless of block location, however, composite 500 hPa geopotential height block centers (Figure 2) are collocated with negative cloud fraction anomalies because of high pressure subsidence (Box et al., 2012; Hanna et al., 2014; Hofer et al., 2017; Lim et al., 2016; Mioduszewski et al., 2016; Rajewicz & Marshall, 2014). In the case of "All Blocks," cloud fraction anomalies are negative over most of the GrIS (Figure 3c). The most negative of these cloud fraction changes is located over southern Greenland and coincides with the average "All Blocks" high pressure center (Figure 2a). In agreement with previous studies (e.g., Delhasse et al., 2018; Hofer et al., 2017), limited positive cloud fraction anomalies in north-central Greenland result from onshore, westerly airflow (Figure 4a) that cools adiabatically and condenses. Overall, Greenland-average (i.e., latitude-weighted average of all GrIS grids) cloud fraction decreases by 0.04 in "All Blocks."

Outside of the block centers for each block location, we find that NW and NE block day cloud fraction change patterns are markedly different from those for SW and SE block days. In these cases, easterly winds flow (Figures 4c–4d) downslope from central Greenland and warm adiabatically to inhibit cloud formation. NW block days also produce significant cloud fraction enhancements over the eastern half of the GrIS (Figure 3d) because of rising northerly airflow (Figure 4c). Despite these small regions of increased cloudiness, Greenland-average cloud fraction is reduced by 0.09 and 0.12 during NW and NE block days, respectively (Figures 3d–3e). Cloud fraction anomaly spatial patterns reverse for SW and SE block days. Namely, SW and SE blocking produce enhanced cloud fractions over portions of western Greenland and cloud fraction reductions over eastern Greenland. Cloud fraction changes for southern Greenland block days more closely represent "All Blocks" cloud fraction changes because they constitute a majority of all block days.

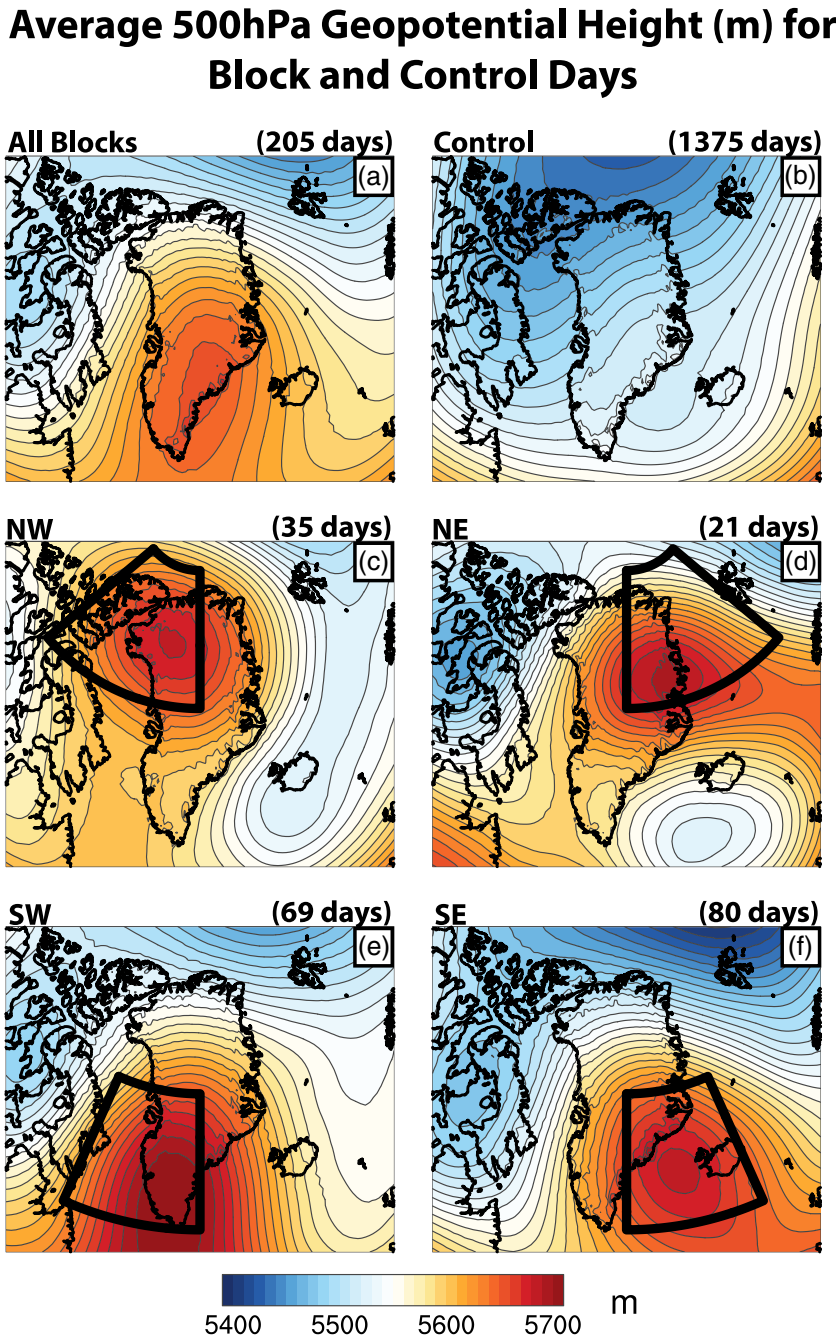

Figure 2. Composite 500 hPa geopotential height plots for (a) "All Blocks," (b) "Control," (c) NW, (d) NE, (e) SW, and (f) SE block days. Day counts are listed above each panel. Black boxes in (c)–(f) represent the corresponding block quadrant boundaries.

Positive cloud fraction anomalies over northern Greenland are produced by westerly based winds moving upslope over the GrIS margins (Figures 4e–4f) that adiabatically enhance cloud cover (i.e., Mattingly et al., 2018; McLeod & Mote, 2015; Mioduszewski et al., 2016; Neff et al., 2014). SE block days reduce cloud fractions along the eastern GrIS margins because westerly airflow adiabatically warms as it descends from the central GrIS toward the eastern shoreline. Similarly for SW block days, we calculate reduced cloud coverage over southeastern Greenland because of downslope airflow. Despite more prevalent cloud fraction enhancement over the GrIS during SE block days, GrIS-average cloud fraction anomalies are still negative (−0.02).

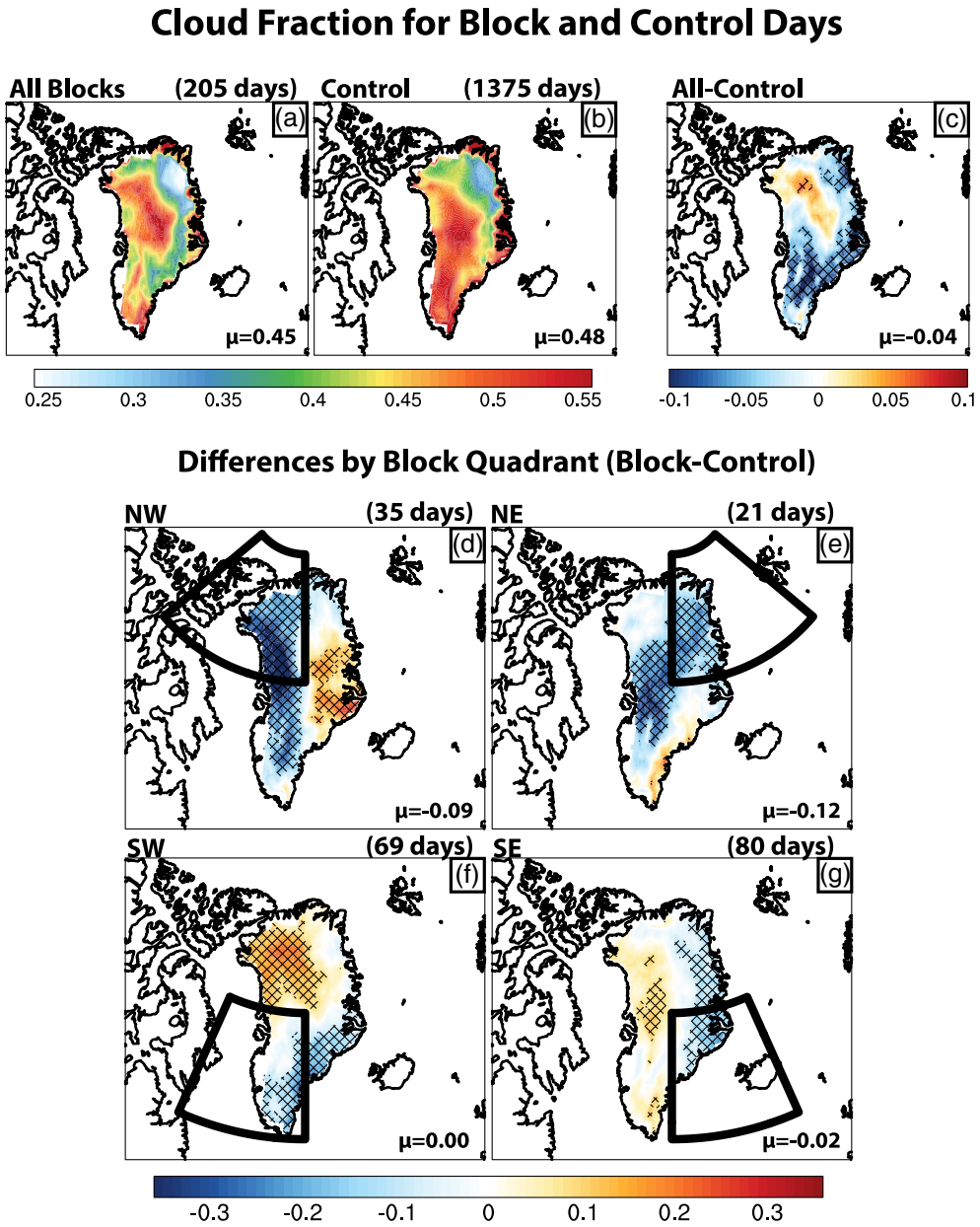

Figure 3. MOD06 cloud fraction. Panels (a) and (b) show absolute cloud fraction for "All Blocks" and "Control," respectively, and their difference is in panel (c). Quadrant-based cloud fraction changes with respect to "Control" are in panels (d) through (g), with GrIS averages (μ) in the lower right-hand corner of each panel. The black boxes are the corresponding quadrant boundaries. Cross-hatching in panels (c) through (g) represents statistically significant differences (95% confidence level).

Cloud water path anomaly patterns (Figure S2) for each blocking case are similar to cloud fraction changes; areas of reduced cloud fraction align with areas of decreased cloud water path, and vice versa. Negative cloud water path changes occur for all block locations despite greater moisture availability relative to "Control" (Table S4) because of subsidence-produced atmospheric stability. However, cloud water path anomalies are more negative for NW and NE block days because their available moisture is sourced from the cold, dry Arctic Ocean and Greenland Sea, respectively (Nusbaumer et al., 2019). In contrast, SW and SE block day moisture is sourced from the warmer North Atlantic Ocean (e.g., Mattingly et al., 2018; McLeod & Mote, 2015; Mioduszewski et al., 2016; Neff et al., 2014). Cloud water path reductions can reduce cloud shortwave scattering (Bennartz et al., 2013) and influence surface cloud radiative forcing.

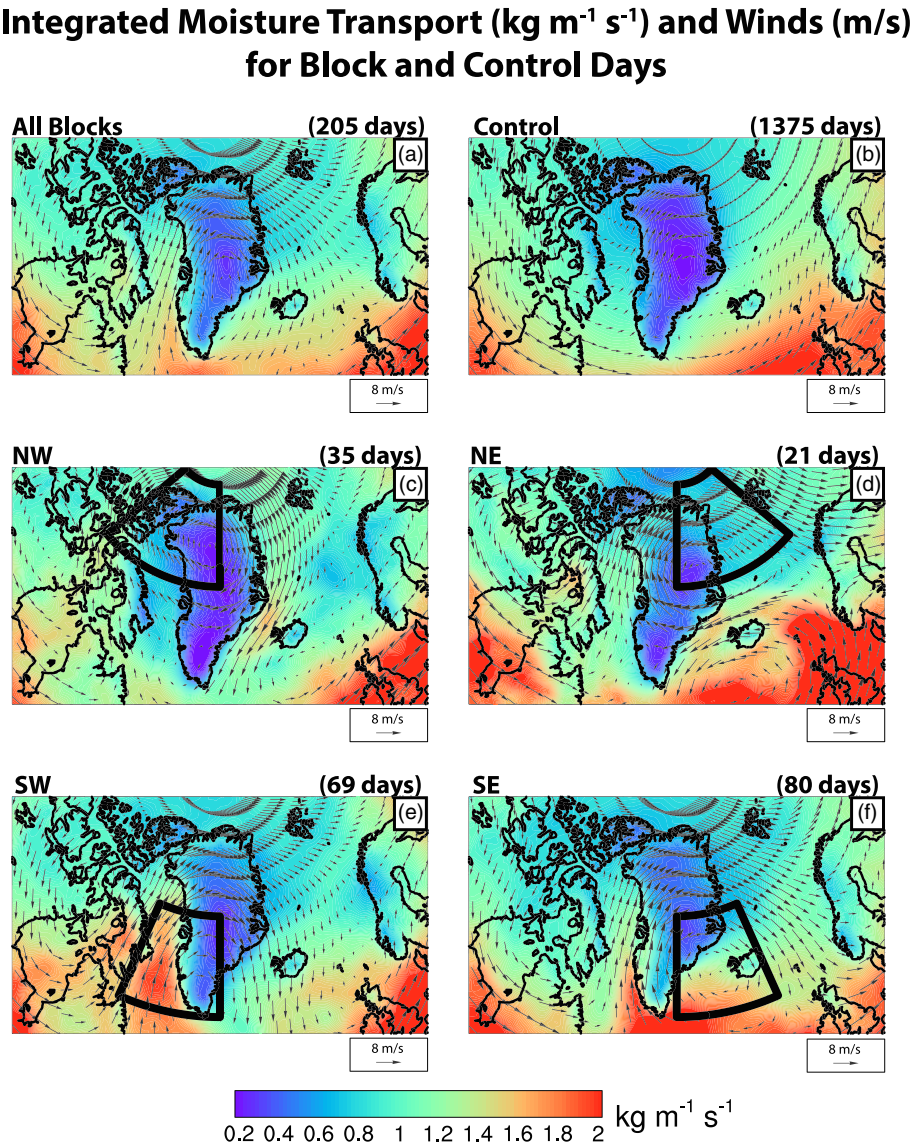

Figure 4. Pressure weighted vertically integrated moisture transport (shading) and winds ($\overrightarrow{W}$; arrows) for (a) "All Blocks," (b) "Control," and (c–f) separate block quadrants. The reference wind speed and arrow size are shown below each panel.

From these results, we can see that cloud anomaly patterns differ by block location, especially between northern quadrant and southern quadrant block days. NW and NE blocking produce greater cloud fraction and cloud water path reductions relative to "Control," especially over western Greenland. In contrast, SW and SE block days enhance (reduce) cloud fraction and cloud water paths over portions of western (eastern) Greenland. These differences arise from (1) persistent, anticyclonic airflow over Greenland's elevated surface and (2) moisture prevalence and source region. As we will see in the following section, cloud properties for different block locations can directly affect energy fluxes received at the surface.

3.3. Cloud Radiative Forcing and Block Location

In the previous section, we found that NW and NE quadrant blocking produce greater GrIS-wide cloud fraction and cloud water path reductions than SW and SE block days. We combine our cloud results with MERRA-2 shortwave and longwave cloud radiative forcing data to investigate the impacts of block location on surface radiative energy. To disentangle the effects of clouds on radiative fluxes, we use clear-sky and all-sky shortwave and longwave fluxes to calculate cloud radiative forcing (Equation 3). Although cloud

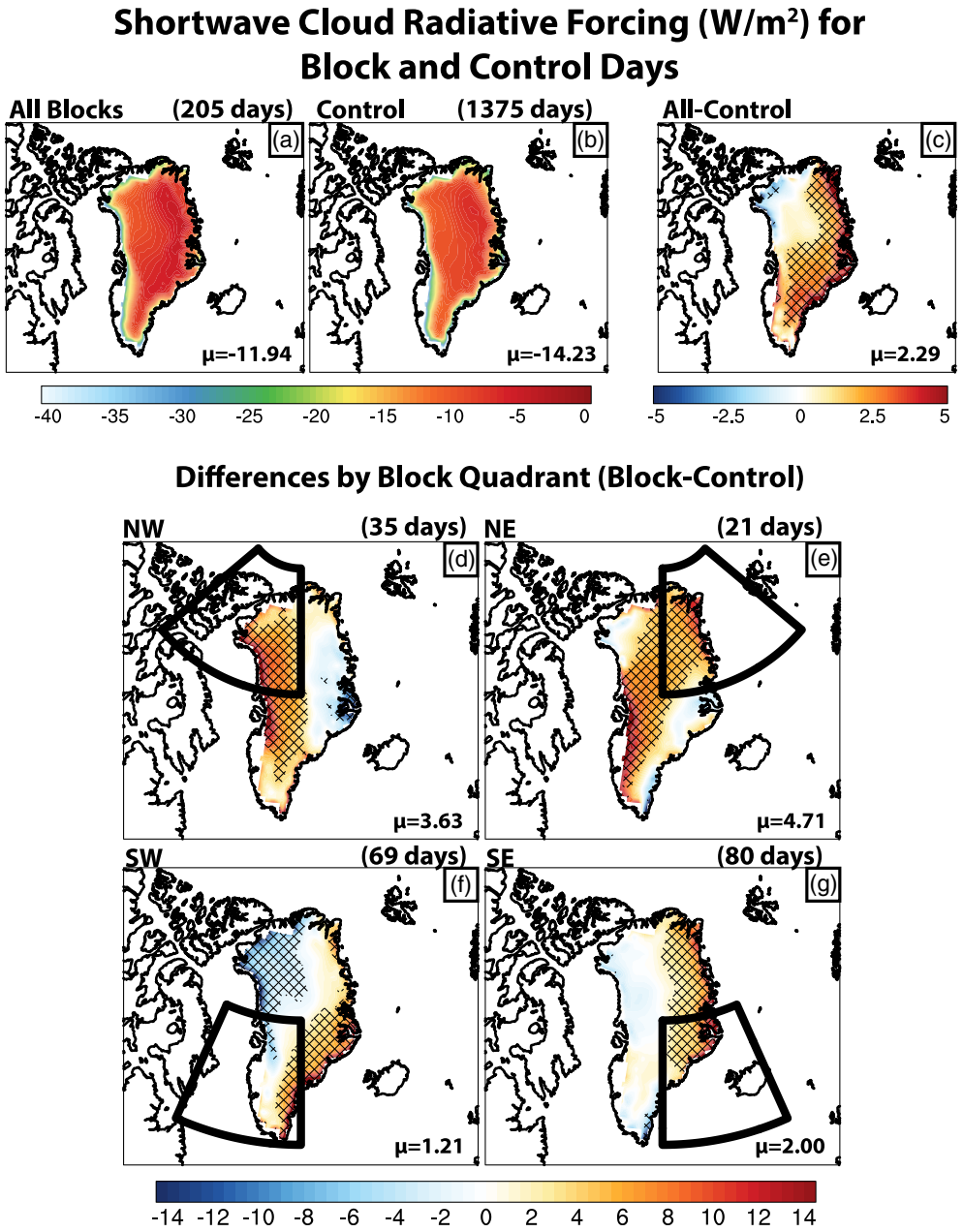

Figure 5. Same as Figure 3, but for MERRA-2 derived surface net shortwave cloud radiative forcing at the surface (W/m^2).

radiative forcing does not account for net surface energy changes, it is a useful metric for explaining radiative impacts of the actual clouds (Intrieri et al., 2002; Wang et al., 2019). All energy fluxes are defined as positive in the downward direction (i.e., into the surface).

Clouds in "All Blocks" and "Control" days produce negative absolute shortwave cloud radiative forcing because of scattering (Figures 5a–5b). However, because cloud fraction and cloud water path reductions in "All Blocks" reduce scattering above the surface, positive shortwave cloud radiative flux anomalies result over most of the GrIS (Figure 5c). Similarly, we find positive (negative) shortwave cloud radiative forcing anomalies for negative (positive) cloud fraction changes in each of the block quadrant cases (Figures 5d–5g). NW and NE block days display significant shortwave cloud radiative forcing enhancements over western Greenland and within their respective block quadrant boundaries, while SW and SE block days

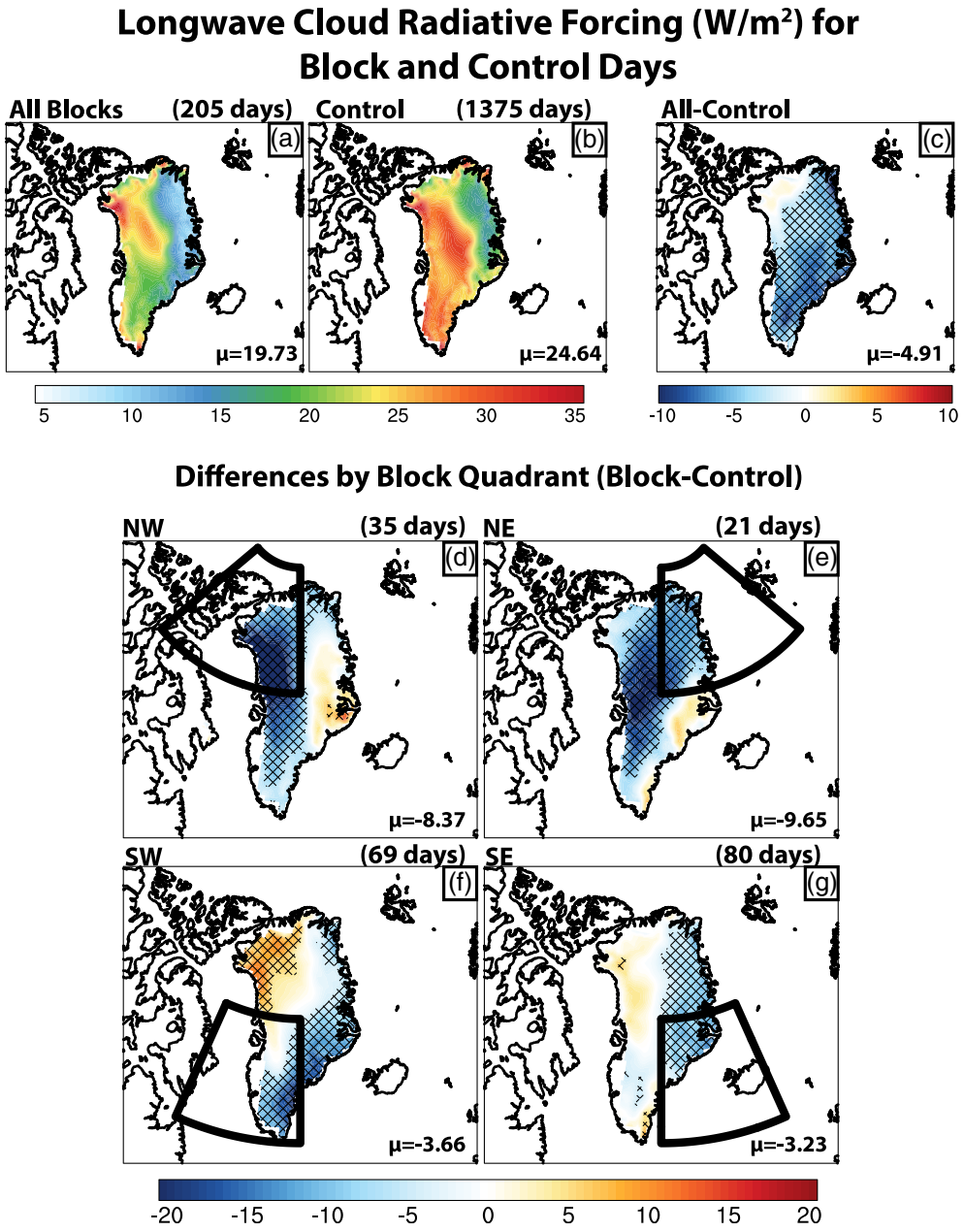

Figure 6. Same as Figure 3, but for MERRA-2 derived surface net longwave cloud radiative forcing at the surface (W/m^2).

exhibit positive shortwave cloud radiative forcing changes over portions of eastern Greenland. Overall, spatially averaged shortwave cloud radiative forcing anomalies are largest during NW and NE block days (+3.63 and +4.71W/m^2 respectively; Figures 5d and 5e).

We see the changes of the opposite sign in longwave surface cloud radiative forcing during blocking (Figure 6). "All Blocks" longwave cloud radiative forcing anomalies are significantly negative over most of the GrIS (Figure 6c). Similarly, blocking in each block quadrant produces negative longwave cloud radiative forcing anomalies in regions of reduced cloudiness. Despite positive atmosphere temperature anomalies during blocking (i.e., Figure S3), reduced cloud cover decreases downwelling longwave energy (i.e., Miller et al., 2015; Shupe & Intrieri, 2004) while surface-based upwelling longwave energy remain approximately constant (not shown), which produces negative changes in net longwave cloud radiative forcing (Lenaerts et al., 2019; van As et al., 2012). Like our shortwave cloud radiative forcing results, we find NW and NE

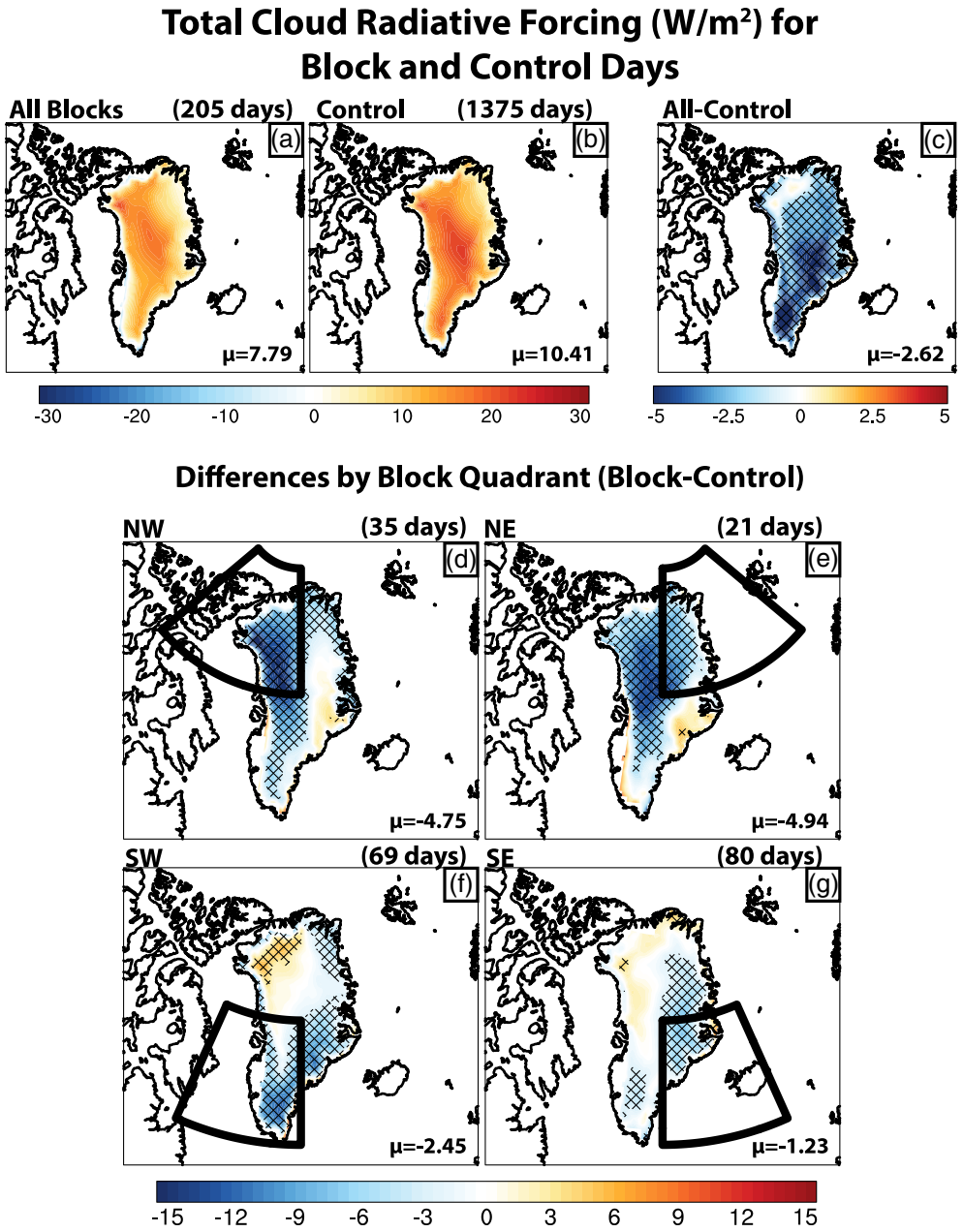

Figure 7. Same as Figure 3, but for MERRA-2 derived total surface cloud radiative forcing.

blocking produce Greenland-average longwave cloud radiative forcing reductions (−8.37 and −9.65W/m^2) that are two to three times greater than those for SW and SE block days because of larger cloud fraction and cloud water path reductions.

When we compute net cloud radiative forcing anomalies for each blocking case (Figure 7), we find that longwave cloud radiative forcing anomalies outweigh shortwave cloud radiative forcing anomalies and result in dominantly negative net cloud radiative forcing. These net cloud radiative forcing anomaly patterns resemble cloud fraction and cloud water path changes during all blocking scenarios. Larger longwave cloud radiative forcing contributions to net cloud radiative forcing anomalies aligns with previous studies on Greenland cloud radiative forcing (Miller et al., 2015; Van Tricht et al., 2016). NW and NE blocks produce the most negative net cloud radiative forcing changes (−4.75 and −4.94W/m^2, respectively) that have magnitudes approximately two times larger than net cloud radiative forcing anomalies for SW and SE block days (−2.45 and −1.23W/m^2).

NW and NE block days exhibit larger positive shortwave cloud radiative forcing anomalies and more negative longwave cloud radiative forcing anomalies than southern quadrant blocking because of greater cloud cover reductions. In the case of shortwave cloud radiative forcing changes, we hypothesize that positive ice cloud fraction (Figure S5) and negative liquid cloud fraction (Figure S4) changes during NE and SE block days also increase net shortwave cloud radiative forcing (compared to NW and SW block days, respectively) by reducing cloud albedo. For each block location, however, longwave cloud radiative forcing changes outweigh shortwave cloud radiative forcing changes, resulting in negative cloud radiative effects over the GrIS because of reduced cloudiness. These findings demonstrate that block location is important not only for cloud changes over Greenland but also for associated cloud radiative forcing anomalies.

3.4. Surface Energy Fluxes and Block Location

Because changes in net surface energy fluxes are impacted by factors other than cloud presence (e.g., air temperature, moisture availability, and surface albedo), we calculate net surface shortwave and longwave flux anomalies for each block location. Overall, Greenland-average net radiative flux (i.e., the sum of net shortwave and net longwave fluxes) increases for all blocking cases (Figures S9 and S10). Net shortwave flux anomalies are especially large over the GrIS margins (Figure S9) because of corresponding albedo reduction. Unlike southern quadrant block days, negative net longwave flux anomalies produced by northern quadrant blocking partially offset positive changes in net shortwave fluxes. SW and SE blocking leads to positive surface shortwave and longwave flux anomalies (SW block day net longwave responses are minimal) because of smaller cloud fraction reductions and moisture transport processes (Figure S10). These positive net radiative flux anomalies correspond to negative Greenland-average total cloud radiative forcing, which highlights the importance of other phenomena apart from clouds for impacting surface radiative fluxes.

Sensible and latent heat fluxes are also important for total surface energy input during blocking. As we can see from Figure 8, significant sensible heat flux anomalies are dominantly positive for all block locations. However, NE and SE block days show larger Greenland-wide sensible heat anomalies (+8.98 and +5.49W/m^2, respectively) than NW and SW block days. Since warm air advection and adiabatic warming of descending airflow have both been shown to contribute to greater downward-directed sensible heat flux (e.g., Box et al., 2012; Fausto et al., 2016; Välisuo et al., 2018), we examine 2 m-temperature anomalies and wind patterns for these cases. All block locations exhibit significantly positive 2 m-temperature anomalies (Figure S3), but the combination of downslope and southerly airflow patterns (Figure 4) onto northern (western) Greenland enhance local warming and produce larger sensible heat flux anomalies during NE (SE) block days. NW and SW blocking, on the other hand, produce northerly and westerly winds that flow upslope toward the central GrIS (Figure 4). These winds cool adiabatically and lead to smaller sensible heat anomalies. Although latent heat flux anomalies are nonnegligible, they are small in comparison with radiative and sensible heat fluxes, so we do not include these findings here (see Figure S11).

Now that we have examined cloud radiative forcing, radiative fluxes, and turbulent heat fluxes associated with different Greenland block locations, we will look at the impact of block location on total surface energy flux (E_{total}), defined as the sum of net shortwave, net longwave, sensible, and latent heat fluxes, respectively:

$$E_{total} = SW_{net} + LW_{net} + SH + LH. \quad (4)$$

We calculate E_{total} for each grid (Figure 9), Greenland-wide averages for each block location (Figure 9), and separate GrIS accumulation and ablation zone averages (Figure 10) to determine how E_{total} changes with elevation. All blocking locations produce large positive surface energy flux changes (Figure 9) corresponding to GrIS margin albedo reduction (Figure S9) that exceed accumulation zone net surface energy anomalies (Figure 10) (e.g., Tedesco et al., 2011). We note that monthly MERRA-2 GrIS surface albedo is consistently smaller than MODIS (i.e., Hall et al., 2018), which could positively bias our net surface energy flux anomaly estimates.

Because runoff and snowmelt dominantly occur in the ablation zone, we focus on energy changes for each block location over lower GrIS elevations. We find that total surface energy anomalies are positive for all block locations, with the largest changes being exhibited by NW and NE block days (+22.33 and +22.50 W/m^2, respectively). Net shortwave anomalies contribute the most to ablation zone net energy changes for all but SE block days (+11.96 to +20.92 W/m^2), followed by sensible heat flux changes (+4.50

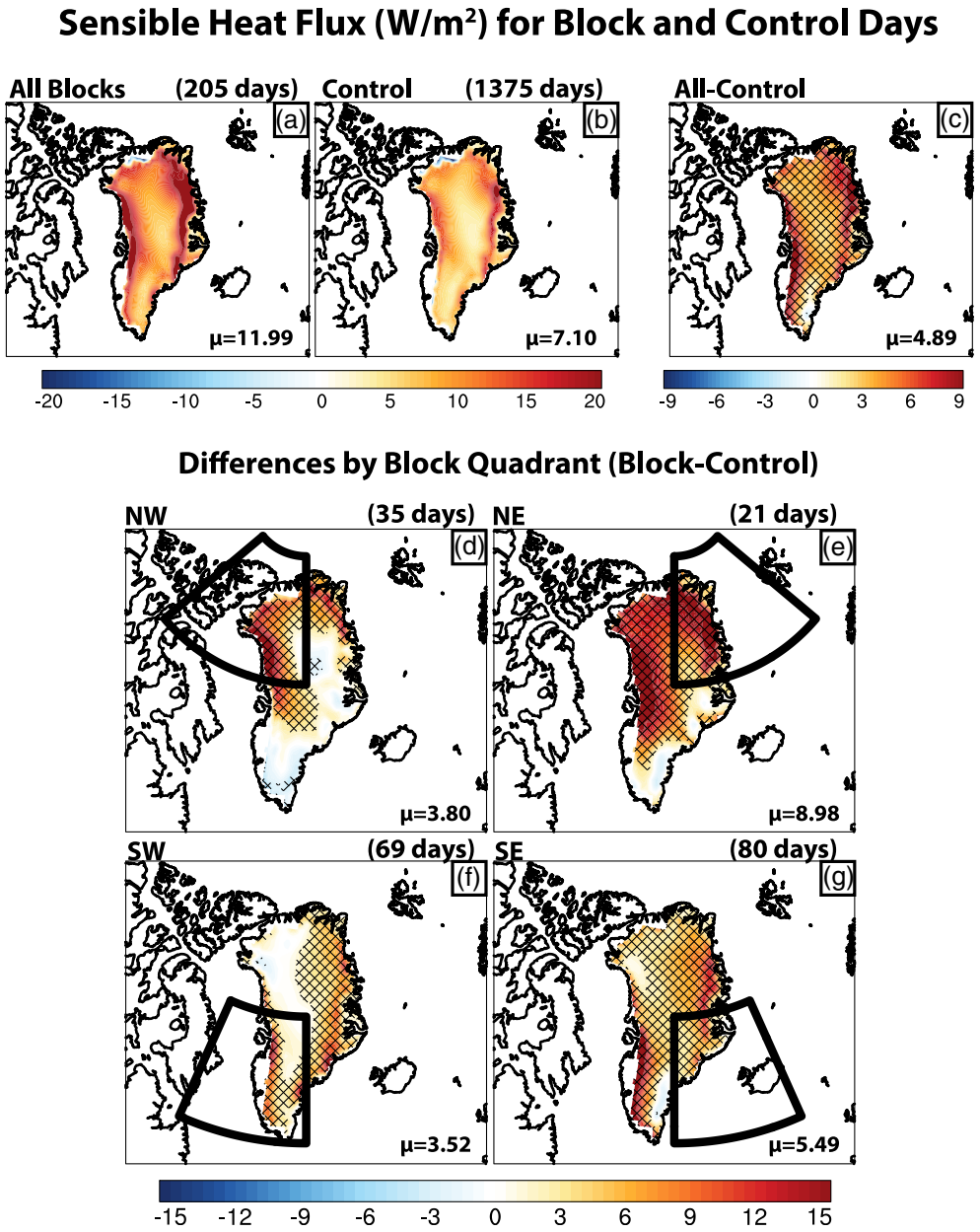

Figure 8. Same as Figure 3, but for MERRA-2 sensible heat flux. Positive quantities are directed into the surface.

to +9.25 W/m^2). In contrast, sensible heating (+6.02 W/m^2) is the largest contributor to SE block quadrant total surface energy change (+12.08 W/m^2). SE block day net longwave energy changes (+3.25 W/m^2) to total surface energy change over the ablation zone. NW, NE, and SW block day net longwave flux changes marginally contribute to total surface energy anomalies.

Relative contributions of component energy flux anomalies that increase total surface energy vary by block quadrant longitude. Sensible heating contributes more to total surface energy enhancement for NE and SE block days (40–50%) than western quadrant block days (20–30%) because of airflow source region. NE and SE blocking activity circulates warmer air from lower latitudes onto the GrIS ablation zone (Figure 4) that enhances sensible heat fluxes relative to western block quadrants at the same latitude. Because airflow is derived from cooler regions for NW and SW block days, net shortwave fluxes along the GrIS margins dominate positive surface changes (70–80%). Net shortwave flux anomalies constitute 10–50% of surface energy enhancement for NE and SE block days.

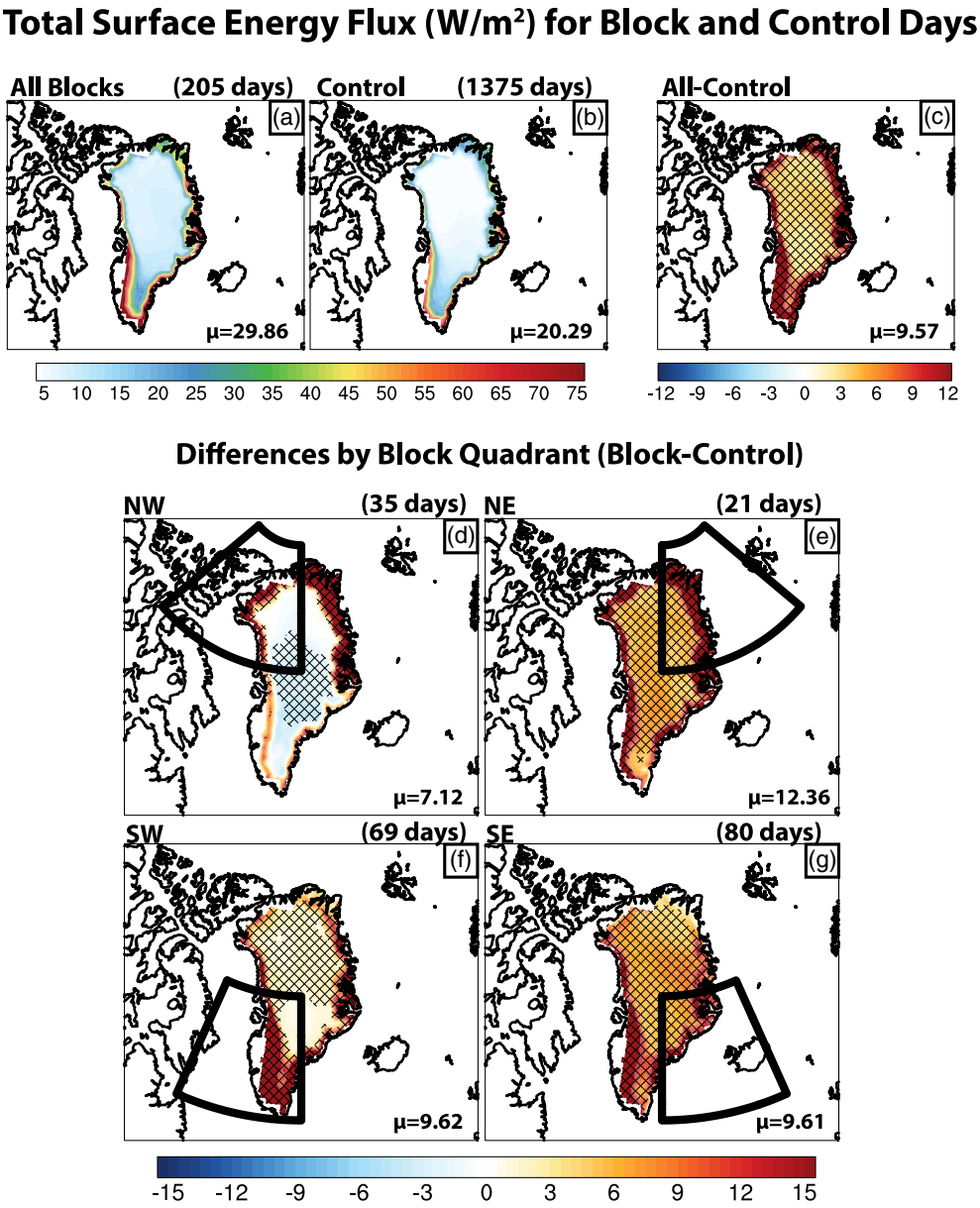

Figure 9. Same as Figure 3, but for MERRA-2 derived total surface energy flux.

Although accumulation zone total surface energy is rarely large enough to trigger melt, surface energy changes can trigger snow aging and reduce surface albedo. We find that, over the GrIS accumulation zone, northerly cold air advection and large cloud reduction result in negative total surface energy anomalies for NW block days (-0.62 W/m^2). All other block locations produce smaller positive total surface energy changes over higher elevations ($+6.04$ to $+8.39$ W/m^2; Figure 10). As a result, NW block days exhibit the lowest Greenland-average net surface flux change ($+7.12$W/m^2) of all block locations. Out of the remaining blocking locations, NE block days exhibit the largest Greenland-wide net surface energy change ($+12.36$W/m^2).

Greenland block location affects spatial and Greenland-average surface energy fluxes through the production of different cloud patterns, moisture transport and source region, and adiabatic heating resulting from orographic airflow. NW block days are unique from other blocking in other locations because they produce negative net surface energy flux anomalies over the central GrIS and result in the lowest Greenland-average net surface energy flux change. Although we find similar total surface energy flux anomaly patterns between the remaining blocking cases, moisture and airflow changes over the GrIS dictate the relative contribution of

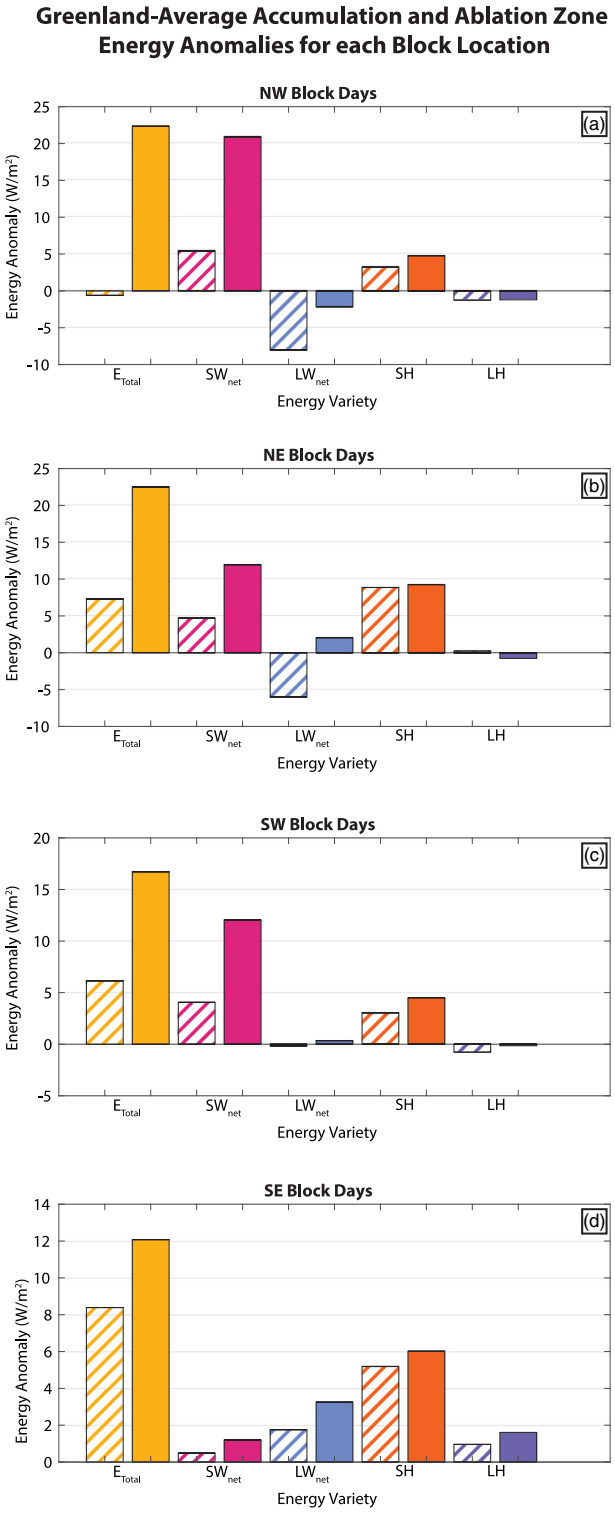

Figure 10. Spatially averaged total surface energy flux, net shortwave, net longwave, sensible heat, and latent heat anomalies separated into accumulation zone (cross-hatched bars, elevations above 1,500 m; e.g., van den Broeke et al., 2008) and ablation zone (elevations below 1,500 m) for (a) NW block days, (b) NE block days, (c) SW block days, and (d) SE block days.

turbulent and radiative heat flux anomalies. Sensible heat fluxes contribute more to net surface energy flux changes for NE and SE block days because of enhanced warm air advection and subsidence over southern and western Greenland. Net solar energy anomalies are the largest contributing energy source to net surface energy changes for NW and SW block days.

4. Conclusions

In this study, we use a combination of MERRA-2 meteorological reanalysis data and MODIS collection 6, level 2 cloud data to assess the impacts of Greenland block location on regional clouds and GrIS surface energy fluxes in the summer months of 2002–2018. We find block days using a modified setup of the D-S block detection algorithm (Dunn-Sigouin et al., 2013) and separate individual block days using uniquely defined equal-area block quadrants over Greenland. We use moisture transport, winds, and temperature data to explain how block location affects clouds and surface energy fluxes and compare these results on a quadrant-by-quadrant basis.

From 2002 through 2018, we find 30 Greenland block events in JJA, totaling 205 block days. Of these years, the summers of 2003, 2006–2008, 2012, and 2015–2016 had higher-than-average block day counts, while our method detects no blocking activity in 2002, 2013, or 2017. Although we verify block activity for each day in our record, we emphasize that block days found by the D-S algorithm (and others) are sensitive to changes in algorithm threshold values. Although most (73%) of these block days are located in the SW and SE block quadrants, understanding cloud and energy flux changes during NW and NE block days (27% of all block days) is also important to fully understanding Greenland blocking.

All Greenland block locations produce negative Greenland-average cloud fraction and cloud water path changes, as demonstrated previously (e.g., Hofer et al., 2017; Lim et al., 2016; Mioduszewski et al., 2016; Tedesco & Fettweis, 2020). However, the extent to which cloud coverage and water path decrease, as well as the cloud change patterns over Greenland, vary by block location. Negative cloud fraction and cloud water path anomalies are at least four times greater for NW and NE block days than SW and SE block days because SW and SE quadrant block days import warmer, moister air over the GrIS to damp the extent of cloud reduction caused by block dynamics.

Cloud radiative forcing anomalies vary in magnitude and spatial distribution for different block locations. Greenland-average shortwave cloud radiative forcing values are greater for NW and NE block days and correspond to large cloud fraction and cloud water path reductions. However, cloud water path changes in eastern Greenland blocks produce greater shortwave cloud radiative forcing anomalies than western Greenland blocks at the same latitude. Longwave cloud radiative forcing and total cloud radiative forcing anomalies are negative for all block locations, with NW and NE block days producing anomalies at least two times as great as SW and SE block day anomalies. Larger longwave cloud radiative forcing anomaly magnitudes indicate that Greenland blocking cloud changes negatively impact the amount of radiative energy absorbed by the surface.

Total surface energy flux anomalies over the entire GrIS vary between block quadrants. Over lower elevations, total surface energy changes are

lower for SW and SE block days relative to northern quadrant blocking. For all block locations except the SE block quadrant, net shortwave and sensible heat flux changes are the greatest contributors to total surface energy anomalies. SE block day total surface energy increases because of sensible heat and net longwave flux changes. NW block days exhibit the least positive Greenland-average net surface energy change ($+7.12 W/m^2$) because of cold air advection and cloud changes over higher elevations. NE blocking produces the greatest Greenland-average net energy flux change ($+12.36 W/m^2$) because of the combined influence of large positive net shortwave and sensible heat flux anomalies. Although net surface energy flux anomalies are similar for each block location, the component flux anomalies that contribute to these changes are different because of changes in dominant air and moisture source regions.

These results all highlight the importance of block location for cloud and surface energy flux patterns over the GrIS. However, some of our chosen methods could affect these findings. One of the most significant constraints in this study is block detection itself. Because there is no concrete definition for blocking, we can justify changes we make to the D-S algorithm thresholds. However, changing these thresholds or using a different detection method to find Greenland blocks from meteorological data could affect the block days identified. Namely, assuming blocks are planetary scale, which is reasonable (e.g., Papritz & Dunn-Sigouin, 2020), the meridional circulation of the block can be linked to vertical motion via the Sverdrup balance (i.e., Wills et al., 2019). Then, stronger blocks will be associated with stronger meridional circulation and vertical cloud motion, yielding potentially greater cloud changes.

This study demonstrates that blocks in northern Greenland more effectively reduce cloud cover and decrease total cloud radiative forcing at the surface. Along with clouds, air temperature, moisture, and surface albedo feedbacks also contribute to surface energy changes during blocking, especially for blocking over southern Greenland that draws warm, moist North Atlantic air over the GrIS. Our findings can be used to further understand the impact of block location on GrIS snowmelt processes through the examination of clouds and surface energy fluxes. Importantly, these results indicate that modeled Greenland responses to blocking should also be sensitive to the simulated block location. Biased block locations in model output could complicate our understanding of the modeled impacts of future blocking on GrIS surface processes.

Data Availability Statement

MODIS Collection 6 data can be accessed online (https://ladsweb.modaps.eosdis.nasa.gov/search/) and MERRA-2 data are downloadable online (https://disc.gsfc.nasa.gov/datasets?keywords=MERRA-2&page=1).

Acknowledgments
We wish to thank the three anonymous reviewers for their helpful feedback. We acknowledge support from NASA Earth and Space Science Fellowship award 80NSSC17K0323.

References

Ackerman, S. A., Strabala, K. I., Menzel, W. P., Frey, R. A., Moeller, C. C., & Gumley, L. E. (1998). Discriminating clear sky from clouds with MODIS. *Journal of Geophysical Research*, *103*(D24), 32,141–32,157. https://doi.org/10.1029/1998JD200032

Ballinger, T. J., Mote, T. L., Mattingly, K., Bliss, A. C., Hanna, E., van As, D., et al. (2019). Greenland ice sheet late-season melt: Investigating multiscale drivers of K-transect events. *The Cryosphere*, *13*, 2241–2257. https://doi.org/10.5194/tc-13-2241-2019

Belleflamme, A., Fettweis, X., & Erpicum, M. (2015). Recent summer Arctic atmospheric circulation anomalies in a historical perspective. *The Cryosphere*, *9*, 53–64. https://doi.org/10.5194/tc-9-53-2015

Bennartz, R., Shupe, M. D., Turner, D. D., Walden, V. P., Steffen, K., Cox, C. J., et al. (2013). July 2012 Greenland melt extent enhanced by low-level liquid clouds. *Nature*, *496*, 83–86. https://doi.org/10.1038/nature12002

Box, J. E., Fettweis, X., Stroeve, J. C., Tedesco, M., Hall, D. K., & Steffen, K. (2012). Greenland ice sheet albedo feedback: Thermodynamics and atmospheric drivers. *The Cryosphere*, *6*(4), 821–839. https://doi.org/10.5194/tc-6-821-2012

Cawkwell, F. G. L., & Bamber, J. L. (2002). The impact of cloud cover on the net radiation budget for the Greenland ice sheet. *Annals of Glaciology*, *34*, 141–149. https://doi.org/10.3189/172756402781817789

Chen, X., & Luo, D. (2017). Arctic sea ice decline and continental cold anomalies: Upstream and downstream effects of Greenland blocking. *Geophysical Research Letters*, *44*, 3411–3419. https://doi.org/10.1002/2016GL072387

Cullather, R. I., & Nowicki, S. M. J. (2018). Greenland ice sheet surface melt and its relation to daily atmospheric conditions. *Journal of Climate*, *31*, 1897–1919. https://doi.org/10.1175/JCLI-D-17-0447.1

Delhasse, A., Fettweis, X., Kittel, C., Amory, C., & Agosta, C. (2018). Brief communication: Impact of the recent atmospheric circulation change in summer on the future surface mass balance of the Greenland ice sheet. *The Cryosphere*, *12*, 3409–3418. https://doi.org/10.5194/tc-12-3409-2018

Dunn-Sigouin, E., Son, S.-W., & Lin, H. (2013). Evaluation of northern hemisphere blocking climatology in the global environment multiscale model. *Monthly Weather Review*, *141*, 707–727. https://doi.org/10.1175/MWR-D-12-00134.1

Edwards-Opperman, J., Cavallo, S., & Turner, D. (2018). The occurrence and properties of long-lived liquid-bearing clouds over the Greenland ice sheet and their relationship to the North Atlantic Oscillation. *Journal of Applied Meteorology and Climatology*, *57*, 921–935. https://doi.org/10.1175/JAMC-D-17-0230.1

Fausto, R. S., van As, D., Box, J. E., Colgan, W., Langen, P. L., & Mottram, R. H. (2016). The implication of nonradiative energy fluxes dominating Greenland ice sheet exceptional ablation area surface melt in 2012. *Geophysical Research Letters*, *43*, 2649–2658. https://doi.org/10.1002/2016GL067720

Fettweis, X., Hanna, E., Lang, C., Belleflamme, A., Erpicum, M., & Gallée, H. (2013). Brief communication: Important role of the mid-tropospheric atmospheric circulation in the recent surface melt increase over the Greenland ice sheet. *The Cyrosphere*, *7*, 241–248. https://doi.org/10.5194/tc-7-241-2013

Fettweis, X., Mabille, G., Erpicum, M., Nicolay, S., & Van den Broeke, M. (2011). The 1958–2009 Greenland ice sheet surface melt and the mid-tropospheric atmospheric circulation. *Climate Dynamics*, *36*(1–2), 139–159. https://doi.org/10.1007/s00382-010-0772-8

Gelaro, R., McCarty, W., Suárez, M. J., Todling, R., Molod, A., Takacs, L., et al. (2017). The Modern-Era Retrospective Analysis for Research and Applications, Version 2 (MERRA-2). *Journal of Climate*, *30*, 5419–5454. https://doi.org/10.1175/JCLI-D-16-0758.1

Häkkinen, S., Hall, D. K., Shuman, C. A., Worthen, D. L., & DiGirolamo, N. E. (2014). Greenland ice sheet melt from MODIS and associated atmospheric variability. *Geophysical Research Letters*, *41*, 1600–1607. https://doi.org/10.1002/2013GL059185

Hall, D. K., Cullather, R. I., DiGirolamo, N. E., Comiso, J. C., Medley, B. C., & Nowicki, S. M. (2018). A multilayer surface temperature, surface albedo, and water vapor product of Greenland from MODIS. *Remote Sensing*, *10*, 555. https://doi.org/10.3390/rs10040555

Hanna, E., Cropper, T. E., Hall, R. J., & Cappelen, J. (2016). Greenland blocking index 1851–2015: A regional climate change signal. *International Journal of Climatology*, *36*, 4847–4861. https://doi.org/10.1002/joc.4673

Hanna, E., Fettweis, X., Mernild, S. H., Cappelen, J., Ribergaard, M. H., Shuman, C. A., et al. (2014). Atmospheric and oceanic climate forcing of the exceptional Greenland ice sheet surface melt in summer 2012. *International Journal of Climatology*, *34*, 1022–1037. https://doi.org/10.1002/joc.3743

Hanna, E., Hall, R. J., Cropper, T. E., Ballinger, T. J., Wake, L., Mote, T., & Cappelen, J. (2018). Greenland blocking index daily series 1851-2015: Analysis of changes in extremes and links with North Atlantic and UK climate variability and change. *International Journal of Climatology*, *38*, 3546–3564. https://doi.org/10.1002/joc.5516

Hofer, S., Tedstone, A. J., Fettweis, X., & Bamber, J. L. (2017). Decreasing cloud cover drives the recent mass loss on the Greenland ice sheet. *Science Advances*, *3*, e1700584. https://doi.org/10.1126/sciadv.1700584

Hofer, S., Tedstone, A. J., Fettweis, X., & Bamber, J. L. (2019). Cloud microphysics and circulation anomalies control differences in future Greenland melt. *Nature Climate Change*, *9*, 523–528. https://doi.org/10.1038/s41558-019-0507-8

Intrieri, J. M., Fairall, C. W., Shupe, M. D., Persson, P. O. G., Andreas, E. L., Guest, P. S., & Moritz, R. E. (2002). An annual cycle of Arctic surface cloud forcing at SHEBA. *Journal of Geophysical Research*, *107*(C10), 8039. https://doi.org/10.1029/2000JC000439

Johansson, E., Devasthale, A., Tjernström, M., Ekman, A. M. L., & L'Ecuyer, T. (2017). Response of the lower troposphere to moisture intrusions into the Arctic. *Geophysical Research Letters*, *44*, 2527–2536. https://doi.org/10.1002/2017GL072687

Lenaerts, J. T. M., Medley, B., van den Broeke, M., & Wouters, B. (2019). Observing and modeling ice sheet surface mass balance. *Reviews of Geophysics*, *57*, 376–420. https://doi.org/10.1029/2018RG000622

Lenaerts, J. T. M., Van Tricht, K., Lhermitte, S., & L'Ecuyer, T. S. (2017). Polar clouds and radiation in satellite observations, reanalyses, and climate models. *Geophysical Research Letters*, *44*, 3355–3364. https://doi.org/10.1002/2016GL072242

Lim, Y.-K., Schubert, S. D., Nowicki, S. M. J., Lee, J. N., Molod, A. M., Cullather, R. I., et al. (2016). Atmospheric summer teleconnections and Greenland ice sheet surface mass variations: Insights from MERRA-2. *Environmental Research Letters*, *11*, 024002. https://doi.org/10.1088/1748-9326/11/2/024002

Liu, Y., Ackerman, S. A., Maddux, B. C., Key, J. R., & Frey, R. A. (2010). Errors in cloud detection over the Arctic using a satellite imager and implications for observing feedback mechanisms. *Journal of Climate*, *23*(7), 1894–1907. https://doi.org/10.1175/2009JCLI3386.1

Mattingly, K. S., Mote, T. L., & Fettweis, X. (2018). Atmospheric river impacts on Greenland ice sheet surface mass balance. *Journal of Geophysical Research: Atmospheres*, *123*, 8538–8560. https://doi.org/10.1029/2018JD028714

Mattingly, K. S., Ramseyer, C. A., Rosen, J. J., Mote, T. L., & Muthyala, R. (2016). Increasing water vapor transport to the Greenland ice sheet revealed using self-organizing maps. *Geophysical Research Letters*, *43*, 9250–9258. https://doi.org/10.1002/2016GL070424

McIlhattan, E. A., L'Ecuyer, T. S., & Miller, N. B. (2017). Observational evidence linking Arctic supercooled liquid cloud biases in CESM to snowfall processes. *Journal of Climate*, *30*, 4477–4495. https://doi.org/10.1175/JCLI-D-16.0666.1

McLeod, J. T., & Mote, T. L. (2015). Assessing the role of precursor cyclones on the formation of extreme Greenland blocking episodes and their impact on summer melting across the Greenland ice sheet. *Journal of Geophysical Research: Atmospheres*, *120*, 12,357–12,377. https://doi.org/10.1002/2015JD023945

McLeod, J. T., & Mote, T. L. (2016). Linking interannual variability in extreme Greenland blocking episodes to the recent increase in summer melting across the Greenland ice sheet. *International Journal of Climatology*, *36*, 1484–1499. https://doi.org/10.1002/joc.4440

Miller, N. B., Shupe, M. D., Cox, C. J., Walden, V. P., Turner, D. D., & Steffen, K. (2015). Cloud radiative forcing at summit, Greenland. *Journal of Climate*, *28*, 6267–6280. https://doi.org/10.1175/JCLI-D-15-0076.1

Mioduszewski, J. R., Rennermalm, A. K., Hammann, A., Tedesco, M., Noble, E. U., Stroeve, J. C., & Mote, T. L. (2016). Atmospheric drivers of Greenland surface melt revealed by self-organizing maps. *Journal of Geophysical Research: Atmospheres*, *121*, 5095–5114. https://doi.org/10.1002/2015JD024550

Neff, W., Compo, G. P., Ralph, F. M., & Shupe, M. D. (2014). Continental heat anomalies and the extreme melting of the Greenland ice surface in 2012 and 1889. *Journal of Geophysical Research: Atmospheres*, *119*, 6520–6536. https://doi.org/10.1002/2014JD021470

Noël, B., van de Berg, W. J., Lhermitte, S., & van den Broeke, M. R. (2019). Rapid ablation zone expansion amplifies north Greenland mass loss. *Science Advances*, *5*, eaaw0123. https://doi.org/10.1126/sciadv.aaw0123

Nusbaumer, J., Alexander, P. M., LeGrande, A. N., & Tedesco, M. (2019). Spatial shift of Greenland moisture sources related to enhanced Arctic warming. *Geophysical Research Letters*, *46*, 14,723–14,731. https://doi.org/10.1029/2019GL084633

Papritz, L., & Dunn-Sigouin, E. (2020). What configuration of the atmospheric circulation drives extreme net and total moisture transport into the Arctic? *Geophysical Research Letters*, *47*, e2020GL089769. https://doi.org/10.1029/2020GL089769

Pfahl, S., Schwierz, C., Croci-Maspoli, M., Grams, C. M., & Wernli, H. (2015). Importance of latent heat release in ascending air streams for atmospheric blocking. *Nature Geoscience*, *8*, 610–614. https://doi.org/10.1038/NGEO2487

Platnick, S., Li, J. Y., King, M. D., Gerber, H., & Hobbs, P. V. (2001). A solar reflectance method for retrieving the optical thickness and droplet size of liquid water clouds over snow and ice surfaces. *Journal of Geophysical Research*, *106*(D14), 15,185–15,199. https://doi.org/10.1029/2000JD900441

Platnick, S., Meyer, K. G., King, M. D., Wind, G., Amarasinghe, N., Marchant, B., et al. (2017). The MODIS cloud optical and microphysical products: Collection 6 updates and examples from Terra and Aqua. *IEEE Transactions on Geoscience and Remote Sensing*, *55*, 502–525. https://doi.org/10.1109/TGRS.2016.2610522

Rajewicz, J., & Marshall, S. J. (2014). Variability and trends in anticyclonic circulation over the Greenland ice sheet, 1948–2013. *Geophysical Research Letters*, *41*, 2842–2850. https://doi.org/10.1002/2014GL059225

Rignot, E., Box, J. E., Burgess, E., & Hanna, E. (2008). Mass balance of the Greenland ice sheet from 1958 to 2007. *Geophysical Research Letters*, *35*, L20502. https://doi.org/10.1029/2008GL035417

Shepherd, A., Ivins, E. R., Geruo, A., Barletta, V. R., Bentley, M. J., Bettadpur, S., et al. (2012). A reconciled estimate of ice-sheet mass balance. *Science*, *338*(6111), 1183–1189. https://doi.org/10.1126/science.1228102

Shupe, M. D., & Intrieri, J. M. (2004). Cloud radiative forcing of the Arctic surface: The influence of cloud properties, surface albedo, and solar zenith angle. *Journal of Climate*, *17*(3), 616–628. https://doi.org/10.1175/1520-0442(2004)017<0616:CRFOTA>2.0.CO;2

Shupe, M. D., Turner, D. D., Walden, V. P., Bennartz, R., Cadeddu, M. P., Castellani, B. B., et al. (2013). High and dry: New observations of tropospheric and cloud properties above the Greenland ice sheet. *Bulletin of the American Meteorological Society*, *94*, 169–186. https://doi.org/10.1175/BAMS-D-11-00249.1

Tedesco, M., & Fettweis, X. (2020). Unprecedented atmospheric conditions (1948–2019) drive the 2019 exceptional melting season over theGreenland ice sheet. *The Cryosphere*, *14*, 1209–1223. https://doi.org/10.5194/tc-14-1209-2020

Tedesco, M., Fettweis, X., Mote, T., Wahr, J., Alexander, P., Box, J. E., & Wouters, B. (2013). Evidence and analysis of 2012 Greenland records from spaceborne observations, a regional climate model and reanalysis data. *The Cryosphere*, *7*, 615–630. https://doi.org/10.5194/tc-7-615-2013

Tedesco, M., Fettweis, X., van den Broeke, M. R., van de Wal, R. S. W., Smeets, C. J. P. P., van de Berg, W. J., et al. (2011). The role of albedo and accumulation in the 2010 melting record in Greenland. *Environmental Research Letters*, *6*, 014005. https://doi.org/10.1088/1748-9326/6/1/014005

Tedesco, M., Mote, T., Fettweis, X., Hanna, E., Jeyaratnam, J., Booth, J. F., et al. (2016). Arctic cut-off high drives the poleward shift of a new Greenland melting record. *Nature Communications*, *7*, 11723. https://doi.org/10.1038/ncomms11723

Välisuo, I., Vihma, T., Pirazzini, R., & Schäfer, M. (2018). Interannual variability of atmospheric conditions and surface melt in Greenland in 2000-2014. *Journal of Geophysical Research: Atmospheres*, *123*, 10,443–10,463. https://doi.org/10.1029/2018JD028445

van As, D., Hubbard, A. L., Hasholt, B., Mikkelsen, A. B., van den Broeke, M. R., & Fausto, R. S. (2012). Large surface meltwater discharge from Kangerlussuaq sector of the Greenland ice sheet during the record-warm year 2010 explained by detailed energy balance observations. *The Cryosphere*, *6*(1), 199–209. https://doi.org/10.5194/tc-6-199-2012

van den Broeke, M., Box, J., Fettweis, X., Hanna, E., Noël, B., Tedesco, M., et al. (2017). Greenland ice sheet surface mass loss: Recent developments in observation and modeling. *Current Climate Change Report*, *3*, 345–356. https://doi.org/10.1007/s40641-017-0084-8

van den Broeke, M., Smeets, P., Ettema, J., van der Veen, C., van de Wal, R., & Oerlemans, J. (2008). Partitioning of melt energy and meltwater fluxes in the ablation zone of the west Greenland ice sheet. *The Cryosphere*, *2*(2), 179–189. https://doi.org/10.5194/tc-2-179-2008

Van Tricht, K., Lhermitte, S., Lenaerts, J. T. M., Gorodetskaya, I. V., L'Ecuyer, T. S., Noël, B., et al. (2016). Clouds enhance Greenland ice sheet meltwater runoff. *Nature Communications*, *7*, 10266. https://doi.org/10.1038/ncomms10266

Wang, W., Zender, C. S., van As, D., & Miller, N. B. (2019). Spatial distribution of melt season cloud radiative effects over Greenland: Evaluating satellite observations, reanalyses, and model simulations against in situ measurements. *Journal of Geophysical Research: Atmospheres*, *124*, 57–71. https://doi.org/10.1029/2018JD028919

Wills, R. C. J., White, R. H., & Levine, X. J. (2019). Northern hemisphere stationary waves in a changing climate. *Current Climate Change Reports*, *5*, 372–389. https://doi.org/10.1007/s40641019-00147-6

Woods, C., Caballero, R., & Svensson, G. (2013). Large-scale circulation associated with moisture intrusions into the Arctic during winter. *Geophysical Research Letters*, *40*, 4717–4721. https://doi.org/10.1002/grl.50912

Woollings, T., Barriopedro, D., Methven, J., Son, S.-W., Martius, O., Harvey, B., et al. (2018). Blocking and its response to climate change. *Current Climate Change Reports*, *4*, 287–300. https://doi.org/10.1007/s40641-018-0108-z

Yang, W., Guo, X., Yao, T., Yang, K., Zhao, L., Li, S., & Zhu, M. (2011). Summertime surface energy budget and ablation modeling in the ablation zone of a maritime Tibetan glacier. *Journal of Geophysical Research*, *116*, D14116. https://doi.org/10.1029/2010JD015183